AIP Advances ARTICLE pubs.aip.org/aip/adv

Tetramethylammonium hydroxide (TMAH) treatment of dry-etched trenches on (010) β-Ga_2O_3 to enhance trench profiles

Cite as: AIP Advances 16, 025145 (2026); doi: 10.1063/5.0305647
Submitted: 16 December 2025 • Accepted: 4 February 2026 •
Published Online: 23 February 2026

Takayoshi Oshima[a)]

AFFILIATIONS

Research Center for Electronic and Optical Materials, National Institute for Materials Science, Tsukuba, Ibaraki 305-0044, Japan

[a)]**Author to whom correspondence should be addressed:** OSHIMA.Takayoshi@nims.go.jp

ABSTRACT

We demonstrated heated tetramethylammonium hydroxide (TMAH) etching (25 wt. % concentration, at 90 °C) as an effective post-dry-etch treatment for improving dry-etched trench profiles on (010) β-Ga_2O_3. This treatment successfully converted rough, tapered dry-etched trench sidewalls into smooth, vertical ones, except for trenches oriented close to the [201] direction, where side etching was most pronounced. In particular, when trenches were oriented along the [102] direction, the exposed vertical sidewalls became exceptionally flat, indicating the preferential development of $(\bar{2}01)$ facets. At the same time, the initially convex trench bottoms were planarized, yielding a well-defined box-like cross-sectional profile. Importantly, both the $(\bar{2}01)$ sidewalls and the (010) bottom surface underwent only minimal material removal, consistent with the very low etch rates of these crystallographic planes. Together with its known ability to alleviate dry-etch damage, TMAH etching can, therefore, be regarded as a highly effective post-treatment for dry-etched fins and trenches on the (010) plane.

β-Ga_2O_3 has recently attracted significant attention as a next-generation ultra-wide-bandgap semiconductor, particularly for future power electronic applications.[1–3] Its exceptionally large critical electric field of ~8 MV cm^{-1} results in a higher Baliga's figure of merit than those of competing wide-bandgap semiconductors such as 4H-SiC and GaN, making it a promising candidate for low-loss and high-power devices.[4] Furthermore, high-quality, scalable wafers can be produced using melt-growth techniques, such as edge-defined film-fed growth,[5] vertical Bridgman,[6] Czochralski,[7] floating zone,[8] and oxide crystal growth from cold crucible[9] methods, which provides a significant advantage over 4H-SiC and GaN that are primarily fabricated by vapor-phase epitaxy. In addition, high-quality films with controlled doping can be grown using conventional epitaxial technologies, including molecular beam epitaxy,[10–12] metal–organic vapor-phase epitaxy,[13,14] and halide vapor-phase epitaxy.[15,16] Moreover, localized n-type and deep-acceptor doping is possible using ion-implantation techniques.[17,18] These bulk and epitaxial growth technologies, combined with doping techniques, enable the realization of device applications. Although the absence of reliable p-type doping limits the device architectures,[19] fundamental n-type unipolar devices [e.g., Schottky barrier diodes (SBDs),[20] trench SBDs,[21] metal–oxide–semiconductor field-effect transistors (MOSFETs),[22] and fin field-effect transistors (FinFETs)][23,24] and bipolar devices [e.g., heterojunction PN diodes (HJ-PND)[25] and super-junction devices (SJ devices)[26]] using alternative p-type oxides, such as NiO, have been demonstrated, underscoring the strong potential of β-Ga_2O_3 for future power device applications.

To further advance the research and development of these devices, studies from multiple perspectives are essential, and the investigation of post-dry-etch treatments is one such direction. Dry etching of β-Ga_2O_3 is primarily performed using Cl-based inductively coupled plasma reactive ion etching (ICP-RIE).[27] This technique is employed not only for mesa formation, which is required for edge termination and device isolation, but also for fine patterning of fins and trenches used in the aforementioned trench SBDs, FinFETs, and SJ devices. However, dry etching generally produces rough surfaces and tapered sidewalls rather than vertical ones.[27]

Moreover, plasma-induced damage introduces numerous electron traps and reduces carrier mobility near the surface, thereby degrading device performance, including increased hysteresis and elevated on-resistance.[28–31] Consequently, the removal of the damaged layer is critical for mitigating these drawbacks and realizing high-performance β-Ga_2O_3 devices. Among the available approaches, wet etching is particularly attractive owing to its process simplicity and effectiveness as a post-dry-etch treatment.[32,33]

Previous studies have suggested that tetramethylammonium hydroxide (TMAH) etching is a promising strategy for post-dry-etch surface treatment. Wet etching using a sulfuric peroxide mixture (SPM), HCl, HF, H_3PO_4, and TMAH has been explored and compared as a method to mitigate plasma-induced damage and surface roughening caused by dry etching.[34–37] Among these options, TMAH has generally proven to be the most effective. Lee *et al.* demonstrated that post-dry-etch treatment with TMAH markedly smoothed the roughened surface of (001) β-Ga_2O_3 following the ICP-RIE process using a Cl_2/BCl_3 gas mixture, whereas SPM yielded only minor improvement.[34] Similarly, Lu *et al.* confirmed that TMAH etching can decrease surface roughness induced by Cl_2/BCl_3-based ICP-RIE.[35] Zhang *et al.* investigated trench SBDs on (001) epitaxial wafers and compared post-dry-etch treatments with O_2 plasma, HF, and TMAH after ICP-RIE with Cl_2/BCl_3 plasma.[36] Their results showed that devices treated with TMAH achieved the highest breakdown voltages, clearly highlighting the advantage of this etchant. Gutierrez *et al.* used x-ray photoelectron spectroscopy to examine (001) epitaxial substrates subjected to ICP-RIE using BCl_3 plasma and subsequently treated with diluted HCl, H_3PO_4, or TMAH.[37] They found that B 1s signals attributed to BCl_3 persisted on HCl- and H_3PO_4-treated surfaces but were absent on TMAH-treated ones, indicating its superior capability for removing damaged layers. Electrical measurements further showed that both SBDs and HJ-PNDs fabricated on TMAH-treated samples exhibited the highest breakdown voltages. In addition, TMAH has been applied to minimize dry-etch damage in recessed-gate and slanted-fin-channel lateral MOSFETs, although detailed results were not reported.[38,39] Beyond its role as a post-dry-etch treatment, TMAH etching serves as an effective pretreatment, capable of producing well-defined step-and-terrace structures on chemically mechanically polished surfaces.[40] Furthermore, it is also used as an undercutting technique to produce air-gap structures, such as cantilevers and air bridges, which are fundamental components of micro-electro-mechanical systems.[41]

Taken together, these findings indicate that TMAH is the most dependable wet-etching solution for β-Ga_2O_3.

However, the effect of TMAH treatment on the morphology of dry-etched sidewalls has not been systematically investigated. In the case of post-dry-etch treatment with H_3PO_4 on (010) β-Ga_2O_3, improvements in sidewall morphology and inclination angle were observed to depend on the crystallographic orientation; however, the physical mechanisms underlying the etching behavior were not discussed.[42] TMAH etching is likewise expected to induce such crystallographic anisotropy-dependent morphological changes. This expectation arises because wet etching of β-Ga_2O_3 in alkaline solutions, including TMAH, proceeds via the following reaction:[43]

$$Ga_2O_3(s) + 2OH^-(aq) + 3H_2O(l) \rightarrow 2\left[Ga(OH)_4\right]^-(aq).$$

In this process, surface Ga atoms are attacked by OH^- ions in the alkaline solution, forming $[Ga(OH)_4]^-$ species that readily dissolve in the solution. As a result, the etching behavior is strongly influenced by the crystal orientation, which determines surface characteristics such as the Ga-to-O ratio (or charge imbalance), dangling-bond density, and surface energy. Therefore, we aimed to clarify the orientation dependence of morphological changes induced by post-dry-etch TMAH treatment. For this purpose, we fabricated trenches by dry etching on (010) β-Ga_2O_3 and examined the anisotropy of the morphological evolution caused by the subsequent TMAH treatment. It should be noted that the (010)-oriented substrate uniquely provides the highest in-plane rotational symmetry (twofold rotational symmetry around the [010] axis) as well as multiple crystallographic planes that are vertically aligned, thereby making it particularly worthy of investigation.

TMAH etching experiments were performed on two (010) β-Ga_2O_3 substrates (sample A and sample B) to determine the (010) etch rate (sample A) and to assess the evolution of trench profiles on the (010) plane (sample B). Figure 1 illustrates the sample preparation sequence. Two substrates with a nominal carrier density of 2.8×10^{18} cm^{-3} (Novel Crystal Technology, Inc.) were coated with a 140-nm-thick SiO_2 masking layer deposited by plasma-enhanced chemical vapor deposition (PECVD). Subsequently, laser lithography was used to define the etch windows. In sample A, only the SiO_2 layer was removed by buffered HF (BHF) to expose the β-Ga_2O_3 surface [Fig. 1(a)], whereas sample B underwent ICP-RIE in a BCl_3/Ar plasma to etch both the SiO_2 layer and the β-Ga_2O_3 substrate, forming β-Ga_2O_3 trenches [Fig. 1(b)]. The dry etch conditions were BCl_3 and Ar flow rates of 50 and 10 sccm, respectively; a chamber pressure of 1.0 Pa; ICP and bias powers of 500 and 30 W, respectively; and an etching time of 10 min. The residual photoresist was removed by sequential cleaning in N-methyl-2-pyrrolidone, isopropyl alcohol,

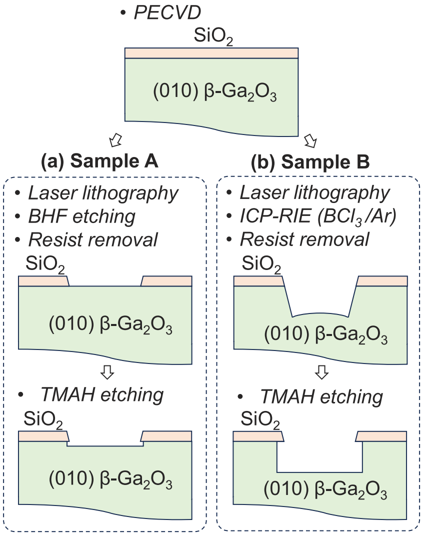

FIG. 1. Schematic illustrations of the process sequence for TMAH etching of (a) a planar surface and (b) dry-etched trenches on (010) β-Ga_2O_3 substrates (corresponding to samples A and B, respectively).

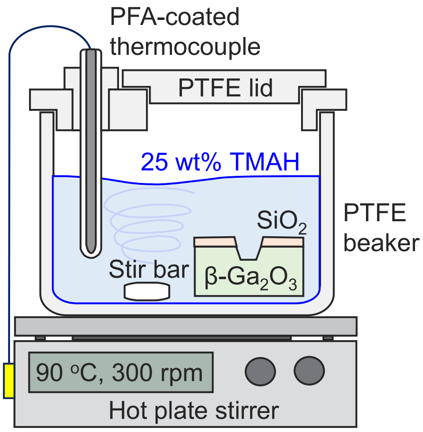

FIG. 2. Schematic diagram of the TMAH etching setup. Although only sample B is depicted in the figure, both samples A and B were etched simultaneously.

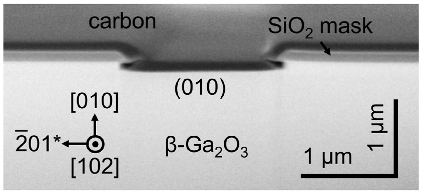

FIG. 3. 54°-tilted cross-sectional SEM image of a TMAH-etched region within an etching window on sample A. The image was acquired at V_{acc} = 2 kV.

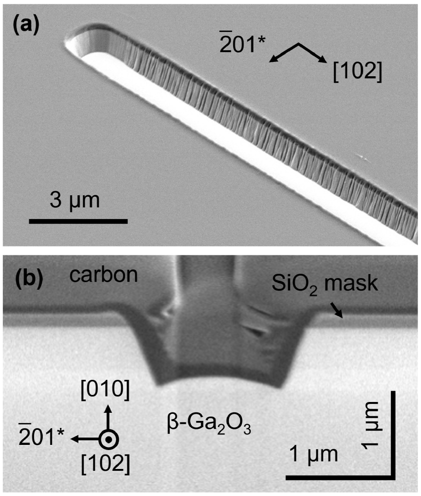

FIG. 4. 54°-tilted SEM images of a dry-etched trench aligned along the [102] direction on sample B. Panels (a) and (b) show surface and cross-sectional views, respectively. All images were acquired at V_{acc} = 2 kV.

and deionized water, followed by oxygen plasma ashing. The BHF-etched depth, excluding the SiO_2 layer, was negligible and consistent with previous reports,[44] whereas the dry-etched depth, excluding the SiO_2 layer, was ~530 nm. Both samples were then wet-etched simultaneously in heated TMAH under the conditions described below.

A 25 wt. % aqueous TMAH solution was used in a polytetrafluoroethylene (PTFE) beaker with a PTFE lid, as shown in Fig. 2. The solution temperature was controlled at 90 °C using a hot-plate stirrer, with a perfluoroalkoxy alkane (PFA)-coated thermocouple immersed in the solution and a small PTFE-coated stir bar rotating at 300 rpm. This temperature was slightly below the solution's boiling point (102 °C). The etching process was initiated by lifting the lid, immersing samples A and B, and then replacing the lid. After wet etching, we removed the lid, retrieved the samples, and rinsed them with deionized water. The etching duration was 90 min.

The resulting etched surface morphologies on the planar surface were evaluated using atomic force microscopy (AFM), while the etched trench structures were investigated using scanning electron microscopy (SEM) and a focused ion beam–scanning electron microscope (FIB–SEM) hybrid system. Cross-sectional observations were performed after site-specific FIB milling. The SEM accelerating voltage (V_{acc}) was set to 2 kV or 10 kV. V_{acc} = 10 kV was used for surface imaging to visualize the side-etched regions through the thin SiO_2 layer and thereby determine the side-etch rate (see Ref. 45 for details), whereas V_{acc} = 2 kV was used in other cases to enhance surface morphology and atomic-number contrast.

Throughout this paper, crystallographic orientations are described using the conventional Miller indices; in addition, the notation hkl^* is introduced to denote the direction perpendicular to the (*hkl*) plane.

The TMAH etch rate of the (010) plane was determined using sample A. Figure 3 shows a cross-sectional SEM image near an etch window after TMAH etching. The TMAH-etched depth was only 0.10 μm, corresponding to an etch rate of 0.07 $\mu m\ h^{-1}$. This very low etch rate on the (010) plane is consistent with a previously reported value of 120 nm h^{-1} obtained using heated H_3PO_4 at 160 °C.[42] Therefore, TMAH etching alone is not a practical approach for patterning (010) β-Ga_2O_3, and dry etching is required for etching in the vertical direction.

However, our dry-etched trenches exhibited non-ideal profiles for device applications. Figure 4 presents an SEM image of a trench after ICP-RIE on sample B. The sidewalls exhibited a rough morphology with numerous striations, most likely originating from the transfer of mask edge features. Moreover, the sidewalls were inclined by 25°–30° relative to the surface normal, while the bottom surface displayed a convex profile, probably as a result of microtrenching induced by ion reflection from the sloped sidewalls.[46] Note that this trench profile did not show any significant in-plane dependence. For the device applications such as FinFETs, the sidewall morphology should be smoothed, the sidewalls made vertical, and the trench bottom planarized. Therefore, we investigated how this undesired dry-etched profile evolves under post-dry-etch TMAH treatment, with particular attention to its anisotropy.

We first investigated the transformation of the surface morphology of the (010) surface on sample B induced by TMAH etching, as shown in Fig. 5. The dry etched surface [Fig. 5(a)] exhibited a smooth surface with a root-mean-square (RMS) roughness of 0.1 nm. However, redeposited particles with heights of 5–50 nm were observed on the surface. These particles were removed by

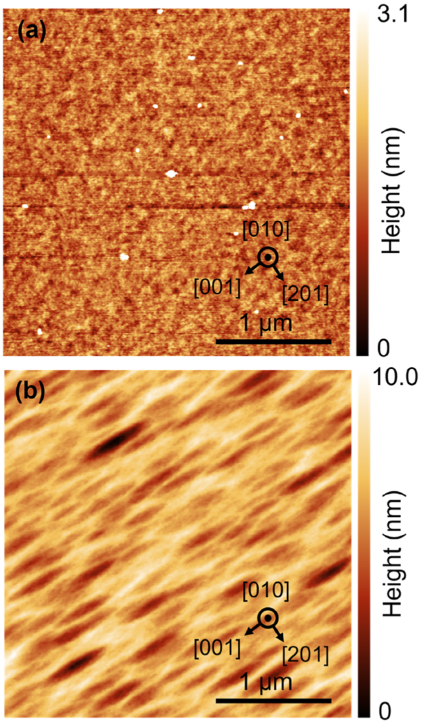

FIG. 5. AFM images of the planar surface of sample B obtained after (a) dry etching and (b) subsequent TMAH treatment.

the subsequent TMAH treatment, but the RMS roughness slightly increased to 1.2 nm owing to the formation of [001]-elongated depressions [Fig. 5(b)]. A similar anisotropic surface morphology was also reported on the (010)-like sidewalls produced by heated H_3PO_4 etching of (001) substrates; therefore, it is a common feature observed in wet etching of the (010) plane.[47]

We then examined the in-plane side-etch characteristics of dry-etched trenches treated with TMAH on sample B. Figure 6 shows the SEM images of the trenches beneath spoke-wheel-shaped etching windows. Two window designs were employed: one with 72 linear windows spaced at 5° intervals [Fig. 6(a)], and the other with windows aligned with specific crystallographic directions—[102], [201], [100], $[10\bar{1}]$, $[10\bar{2}]$, and $[00\bar{1}]$—parallel to the vertically aligned, low-index $(\bar{2}01)$, $(\bar{1}02)$, (001), (101), (201), and (100) planes, respectively [Fig. 6(b)]. In both designs, the window dimensions were 50 μm in length and 1.6 μm in width. Figure 6(c) presents an enlarged view of Fig. 6(a), clearly showing side-etched regions outlined by mask edges and etching fronts. In this study, the side-etch length—measured perpendicular to each linear window—was defined as the distance between the observed mask edge and side-etch front.

Side etching was anisotropic, reflecting the crystal structure of β-Ga_2O_3. Pronounced side etching was observed in trenches oriented close to the [201] and equivalent $[\bar{2}0\bar{1}]$ directions [Figs. 6(a) and 6(b)]. The amount of side etching decreased as the orientation shifted away from these directions. This in-plane variation exhibited twofold rotational symmetry, consistent with the intrinsic twofold symmetry about the [010] axis of the monoclinic crystal structure. Furthermore, in regions with pronounced side etching, straight etching fronts along the [102] and [100] directions were clearly observed near the trench ends [see the purple and red arrows representing the [102] and [100] directions, respectively, in Fig. 6(c)]. These directions are parallel to the vertically aligned $(\bar{2}01)$ and (001) planes, respectively, suggesting the formation of these facet planes. Moreover, shallow linear striations along the [001] direction were observed on the etched bottom surface [see the blue arrows representing the [001] direction in Fig. 6(c)], which is consistent with the surface morphology observed with AFM.

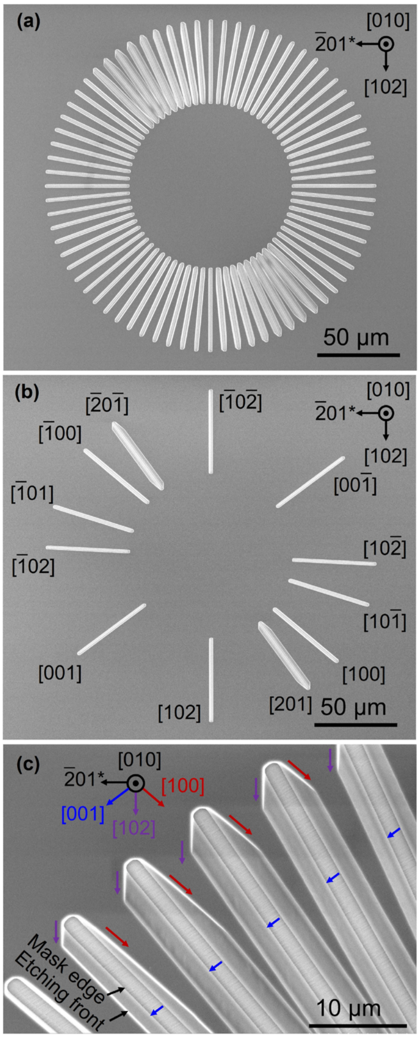

FIG. 6. Top-view SEM images of TMAH-treated trenches formed beneath spoke-wheel-shaped windows (a) with orientations at 5° intervals and (b) aligned with specific crystallographic orientations on sample B. (c) Magnified view of (a), showing trenches with pronounced side etching. All images were acquired at V_{acc} = 10 kV.

We further quantified the in-plane anisotropy of the side-etch rate. Figure 7 shows the polar plots of the extracted side-etch

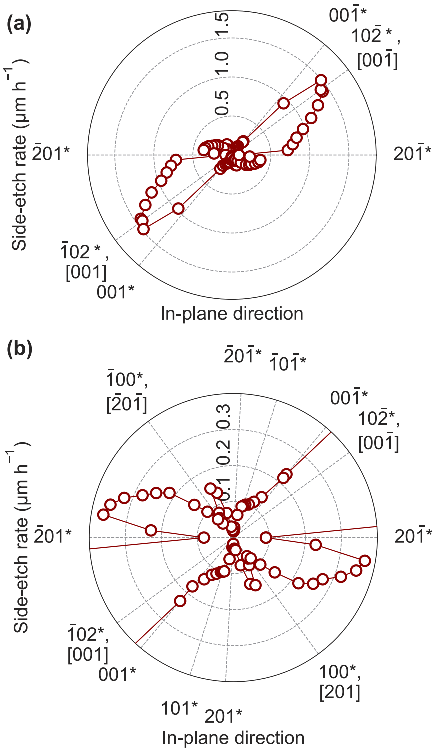

FIG. 7. Polar plots of side-etch rates for (a) the overall rate range and (b) the lower rate range on sample B.

rates measured from the spoke-wheel-shaped trenches depicted in Figs. 6(a) and 6(b). The side etch rate was maximized at ~1.5 μm h^{-1} in the directions close to the [001] and $[00\bar{1}]$ orientations [i.e., directions perpendicular to the $(\bar{1}02)$ plane], while it decreased as the orientation deviated from these directions [Fig. 7(a)]. Notably, it dropped substantially in the directions perpendicular to the $(\bar{2}01)$ and (001) planes, with relatively low rates of 0.09 and 0.20 μm h^{-1}, respectively. These sharp reductions in etch rate explain why distinct linear etching fronts were observed along the [102] and [100] directions in Fig. 6(c). For the lower side-etch rate range (<0.4 μm h^{-1}), there were other in-plane directions that also exhibited local minima [Fig. 7(b)]. These directions were perpendicular to the (201) and (100) planes, with etch rates of ~0.02 and ~0.06 μm h^{-1}, respectively. In the reported H_3PO_4 etching study, the etch rates along the [001] and $[00\bar{1}]$ directions were high, consistent with our TMAH results; however, unlike in our case, the etch rates along the [201] and $[\bar{2}0\bar{1}]$ directions were also high.[42] This discrepancy is likely attributable to differences in the etchants.

Then, we evaluated the morphology of TMAH-treated trench sidewalls. Figure 8 shows the 54°-tilted SEM images of trenches aligned with specific crystal orientations, as indicated in Fig. 6(b). The observable sidewall area depended on the degree of side etching. In the [201]-oriented trench, the side etching was so extensive that the sidewall surface was no longer visible in the tilted view [Fig. 8(b)]. For trenches with other orientations, the sidewall was visible due to the much less extensive side etching, allowing evaluation of its surface morphology. An extremely flat sidewall was observed for the [102] trench [Fig. 8(a)], while a nearly flat sidewall was observed for the [100] trench [Fig. 8(c)], suggesting well-developed $(\bar{2}01)$ and (001) facets, respectively. In contrast, smooth but not flat sidewalls were observed for the $[10\bar{1}]$, $[10\bar{2}]$, and $[00\bar{1}]$ trenches [Figs. 8(d)–8(f)], indicating insufficient development of the (101), (201), and (100) facets, respectively. This trend in sidewall surface flatness cannot be explained solely by differences in the corresponding side-etch rates, since the side-etch rates of the $(\bar{2}01)$ and (001) sidewalls (0.09–0.20 μm h^{-1}) were comparable to or exceeded those of the (101), (201), and (100) sidewalls (0.02–0.10 μm h^{-1}) [Fig. 7(b)]. An additional condition appears necessary for effective sidewall flattening: the side-etch rate in the vicinal directions adjacent to the corresponding facets must be sufficiently high to remove the slanted, rough sidewalls produced by dry etching. For example, the side-etch rate of the $(\bar{2}01)$ sidewall was 0.09 μm h^{-1}, whereas the rates in directions slightly deviated by +(5–10)° and −(5–10)° increased to 0.72–0.79 and 0.23–0.37 μm h^{-1}, respectively [Fig. 7], thereby effectively eliminating the slanted, rough features and exposing the $(\bar{2}01)$ facet. The emergence of flat $(\bar{2}01)$ facets was also reported in etch pitting of (010) and (100) β-Ga_2O_3 substrates using H_3PO_4, where deep, hole-like etch pits formed at defect sites were primarily bounded by flat $(\bar{2}01)$ facets.[48,49] Therefore, the formation of flat $(\bar{2}01)$ facets appears to be a characteristic feature of wet etching. The clear development of the $(\bar{2}01)$ facets is also consistent with the atomic arrangement on the $(\bar{2}01)$ plane. The $(\bar{2}01)$ plane comprises only Ga or only O atoms without any vertical (out-of-plane) displacement, which is unique among crystallographic planes oriented perpendicular to the (010) surface. As a result, a repulsive interaction is expected between OH^- ions and the O-terminated $(\bar{2}01)$ surface,[33] leading to a slow etch rate and the formation of the smooth $(\bar{2}01)$ facets. In contrast, the observed pronounced side etching along the [001] and $[00\bar{1}]$ directions [i.e., directions perpendicular to the $(\bar{1}02)$ plane] is likely attributable to the fact that the $(\bar{1}02)$ plane consists of both Ga and O atoms in a 2:3 ratio, without any vertical (out-of-plane) displacement, which is also unique among crystallographic planes oriented perpendicular to the (010) surface and is, therefore, charge neutral, thereby minimizing the repulsive interaction and enhancing wet etching.

Subsequently, we examined the cross-sectional profiles of TMAH-treated trenches oriented along the specific crystal directions, as shown in Fig. 9. The sidewalls of the [201]-oriented trench were strongly tapered, even more severely than those of the initial dry-etched trench [Fig. 9(b)]. This trend has also been reported for H_3PO_4 etching of dry-etched trenches on (010) β-Ga_2O_3.[42] Thus, this orientation trench is unsuitable for device applications. By contrast, the [102]-, [100]-, $[10\bar{1}]$-, $[10\bar{2}]$-, and $[00\bar{1}]$-trenches exhibited vertical sidewalls, indicating the formation of the $(\bar{2}01)$, (001), (101), (201), and (100) facets, respectively [Figs. 9(a) and 9(c)–9(f)]. However, for the $[00\bar{1}]$ trench, the center of the bottom surface remained convex, indicating insufficient planarization [Fig. 9(f)], because this trench orientation is parallel to the direction of pronounced side-etching. In contrast, the [102]-, [100]-, $[10\bar{1}]$-, and $[10\bar{2}]$ trenches exhibited a relatively flat bottom surface, resulting in a box-like cross-sectional profile. Notably, such complete verticalization was not achieved in H_3PO_4 etching on (010) β-Ga_2O_3,[42] suggesting the superiority of TMAH over H_3PO_4.

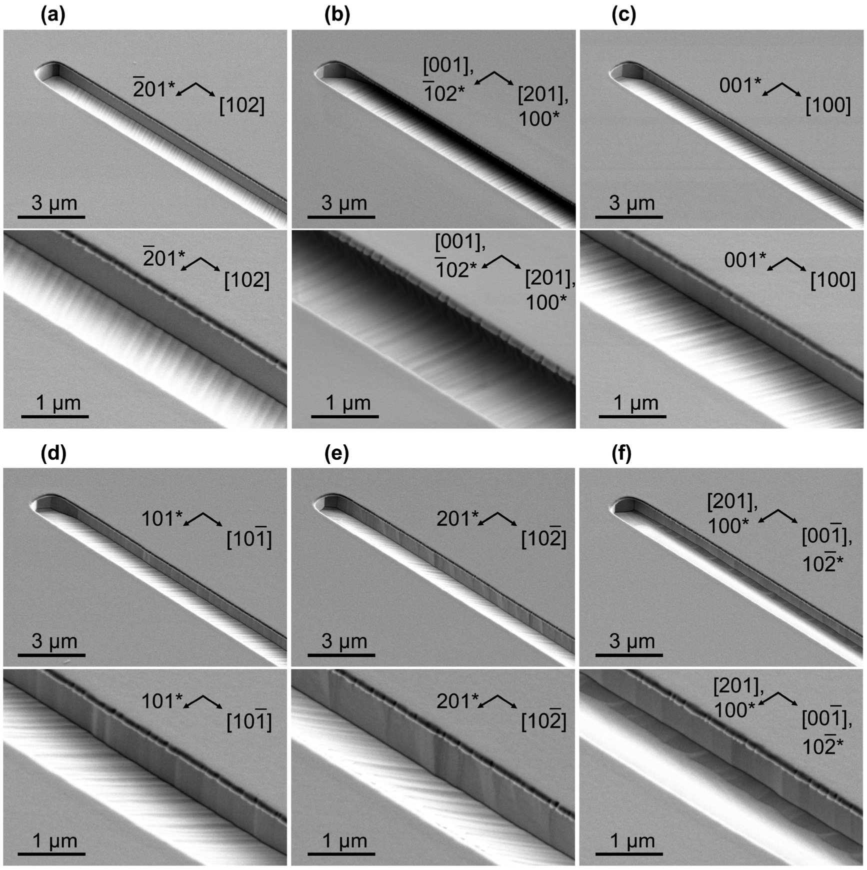

FIG. 8. (a)–(f) 54°-tilted SEM images, acquired at two different magnifications, of TMAH-treated trenches aligned with the specific crystal orientations shown in Fig. 6(b). All images were acquired at V_{acc} = 2 kV.

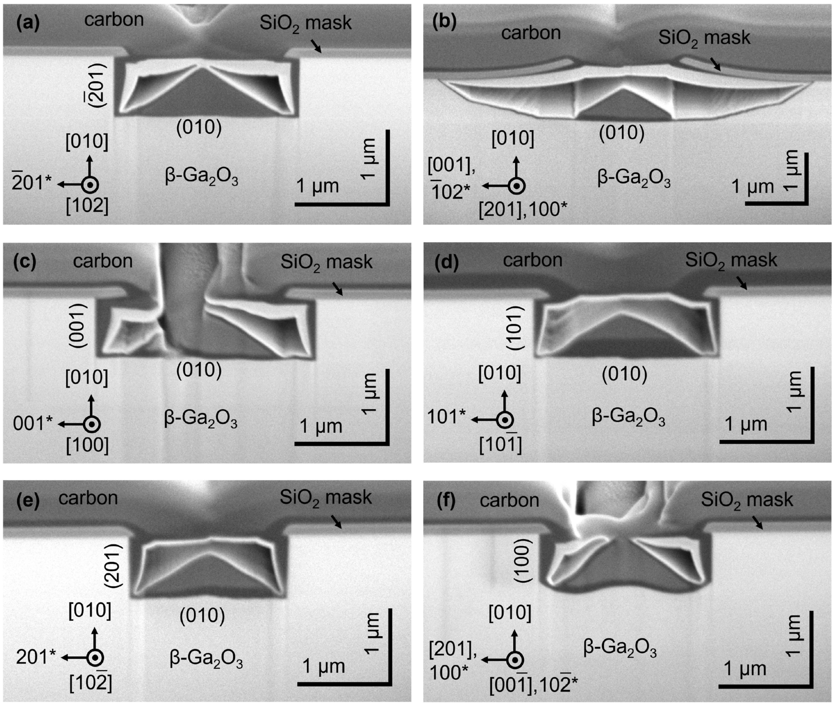

FIG. 9. (a)–(f) 54°-tilted cross-sectional SEM images of TMAH-treated trenches shown in Figs. 8(a)–8(f), respectively. All images were acquired at V_{acc} = 2 kV.

From the standpoints of the sidewall morphology and cross-sectional profile, the [102]-oriented trench is considered particularly suitable for device applications. The striated and tilted sidewalls generated by dry etching were effectively eliminated, exposing perfectly flat and strictly vertical $(\bar{2}01)$-faceted sidewalls [Figs. 8(a) and 9(a)]. In addition, the trench bottom was planarized. It should be noted that the sidewalls and the bottom surface were only minimally etched, owing to the very low etch rates of the $(\bar{2}01)$ and (010) planes (0.09 and 0.07 μm h^{-1}, respectively). Therefore, this post-dry-etch treatment is highly advantageous for the [102] trench, as it improves the morphology of the dry-etched trench without significantly altering its initial width and depth.

In summary, we verified the effectiveness of heated TMAH treatment for dry-etched trenches on (010) β-Ga_2O_3. Although the trench orientation was limited to the [102] direction, an ideal trench profile characterized by perfectly flat and vertical $(\bar{2}01)$ sidewalls and a horizontal bottom surface was obtained through the post-dry-etch treatment, even when the initial dry-etched trench profile was far from the box-like shape. In addition to this shape transformation, TMAH treatment also removes dry-etched damage, thereby improving device performance. At the present stage of device development, such post-dry-etch treatment is expected to be particularly beneficial for the fabrication of FinFETs on (010) β-Ga_2O_3, and evaluating its effectiveness through electrical characteristics will be the focus of our future work.

This study was supported by the Electron Microscopy Unit and the Nanofabrication Unit at the National Institute for Materials Science (NIMS) within the framework of the Advanced Research Infrastructure for Materials and Nanotechnology (ARIM), supported by the Ministry of Education, Culture, Sports, Science and Technology (MEXT), Japan (Grant No. JPMXP1225NM5079). This work was financially supported by a Grant-in-Aid for Scientific Research (B) from the Japan Society for the Promotion of Science (JSPS), MEXT, Japan (Grant No. JP24K01368).

AUTHOR DECLARATIONS

Conflict of Interest

The author has no conflicts to disclose.

Author Contributions

Takayoshi Oshima: Conceptualization (lead); Methodology (lead); Writing – original draft (lead).

DATA AVAILABILITY

The data that support the findings of this study are available from the corresponding author upon reasonable request.

REFERENCES

[1] M. Higashiwaki, IEEE Electron Devices Mag. **2**, 42-C3 (2024).

[2] K. Sasaki, Appl. Phys. Express **17**, 090101 (2024).

[3] S. J. Pearton, F. Ren, A. Y. Polyakov, A. Haque, M. Labed, and Y. S. Rim, Appl. Phys. Rev. **12**, 031336 (2025).

[4] M. Higashiwaki, K. Sasaki, A. Kuramata, T. Masui, and S. Yamakoshi, Appl. Phys. Lett. **100**, 013504 (2012).

[5] A. Kuramata, K. Koshi, S. Watanabe, Y. Yamaoka, T. Masui, and S. Yamakoshi, Jpn. J. Appl. Phys. **55**, 1202A2 (2016).

[6] E. Ohba, T. Kobayashi, T. Taishi, and K. Hoshikawa, J. Cryst. Growth **556**, 125990 (2021).

[7] Z. Galazka, K. Irmscher, R. Uecker, R. Bertram, M. Pietsch, A. Kwasniewski, M. Naumann, T. Schulz, R. Schewski, D. Klimm, and M. Bickermann, J. Cryst. Growth **404**, 184–191 (2014).

[8] E. G. Víllora, K. Shimamura, Y. Yoshikawa, K. Aoki, and N. Ichinose, J. Cryst. Growth **270**, 420–426 (2004).

[9] A. Yoshikawa, V. Kochurikhin, T. Tomida, I. Takahashi, K. Kamada, Y. Shoji, and K. Kakimoto, Sci. Rep. **14**, 14881 (2024).

[10] T. Oshima, N. Arai, N. Suzuki, S. Ohira, and S. Fujita, Thin Solid Films **516**, 5768–5771 (2008).

[11] K. Sasaki, A. Kuramata, T. Masui, E. G. Víllora, K. Shimamura, and S. Yamakoshi, Appl. Phys. Express **5**, 035502 (2012).

[12] K. Azizie, F. V. E. Hensling, C. A. Gorsak, Y. Kim, N. A. Pieczulewski, D. M. Dryden, M. K. I. Senevirathna, S. Coye, S.-L. Shang, J. Steele, P. Vogt, N. A. Parker, Y. A. Birkhölzer, J. P. McCandless, D. Jena, H. G. Xing, Z.-K. Liu, M. D. Williams, A. J. Green, K. Chabak, D. A. Muller, A. T. Neal, S. Mou, M. O. Thompson, H. P. Nair, and D. G. Schlom, APL Mater. **11**, 041102 (2023).

[13] J. Yoshinaga, H. Tozato, T. Okuyama, S. Sasaki, G. Piao, K. Ikenaga, K. Goto, Y. Ban, and Y. Kumagai, Appl. Phys. Express **16**, 095504 (2023).

[14] J. Yoshinaga, Y. Iba, K. Kubota, Y. Terauchi, T. Okuyama, S. Sasaki, K. Ikenaga, T. Onuma, M. Higashiwaki, K. Shiina, S. Koseki, Y. Ban, and Y. Kumagai, Appl. Phys. Express **18**, 055503 (2025).

[15] H. Murakami, K. Nomura, K. Goto, K. Sasaki, K. Kawara, Q. T. Thieu, R. Togashi, Y. Kumagai, M. Higashiwaki, A. Kuramata, S. Yamakoshi, B. Monemar, and A. Koukitu, Appl. Phys. Express **8**, 015503 (2015).

[16] K. Goto, K. Konishi, H. Murakami, Y. Kumagai, B. Monemar, M. Higashiwaki, A. Kuramata, and S. Yamakoshi, Thin Solid Films **666**, 182–184 (2018).

[17] K. Sasaki, M. Higashiwaki, A. Kuramata, T. Masui, and S. Yamakoshi, Appl. Phys. Express **6**, 086502 (2013).

[18] M. H. Wong, C.-H. Lin, A. Kuramata, S. Yamakoshi, H. Murakami, Y. Kumagai, and M. Higashiwaki, Appl. Phys. Lett. **113**, 102103 (2018).

[19] J. L. Lyons, Semicond. Sci. Technol. **33**, 05LT02 (2018).

[20] K. Konishi, K. Goto, H. Murakami, Y. Kumagai, A. Kuramata, S. Yamakoshi, and M. Higashiwaki, Appl. Phys. Lett. **110**, 103506 (2017).

[21] F. Otsuka, H. Miyamoto, A. Takatsuka, S. Kunori, K. Sasaki, and A. Kuramata, Appl. Phys. Express **15**, 016501 (2022).

[22] M. H. Wong, K. Sasaki, A. Kuramata, S. Yamakoshi, and M. Higashiwaki, IEEE Electron Device Lett. **37**, 212–215 (2016).

[23] W. Li, K. Nomoto, Z. Hu, T. Nakamura, D. Jena, and H. G. Xing, "Single and multi-fin normally-off Ga_2O_3 vertical transistors with a breakdown voltage over 2.6 kV," in *2019 IEEE International Electron Devices Meeting* (IEEE, 2019), pp. 12.4.1–12.4.4.

[24] Z. Wang, S. Kumar, T. Kamimura, H. Murakami, Y. Kumagai, and M. Higashiwaki, Jpn. J. Appl. Phys. **63**, 100902 (2024).

[25] F. Zhou, H. Gong, M. Xiao, Y. Ma, Z. Wang, X. Yu, L. Li, L. Fu, H. H. Tan, Y. Yang, F.-F. Ren, S. Gu, Y. Zheng, H. Lu, R. Zhang, Y. Zhang, and J. Ye, Nat. Commun. **14**, 4459 (2023).

[26] Y. Qin, M. Porter, M. Xiao, Z. Du, H. Zhang, Y. Ma, J. Spencer, B. Wang, Q. Song, K. Sasaki, C.-H. Lin, I. Kravchenko, D. P. Briggs, D. K. Hensley, M. Tadjer, H. Wang, and Y. Zhang, "2 kV, 0.7 mΩ cm^2 vertical Ga_2O_3 superjunction schottky rectifier with dynamic robustness," in *2023 International Electron Devices Meeting* (IEEE, 2023), pp. 1–4.

[27] J. E. Hogan, S. W. Kaun, E. Ahmadi, Y. Oshima, and J. S. Speck, Semicond. Sci. Technol. **31**, 065006 (2016).

[28] Z. Wang, X. Yu, H. Gong, T. Hu, Y. Zhang, X. Ji, F. Ren, S. Gu, Y. Zheng, R. Zhang, A. Y. Kuznetsov, and J. Ye, J. Phys. Chem. Lett. **13**, 7094–7099 (2022).

[29] K. D. Chabak, N. Moser, A. J. Green, D. E. Walker, S. E. Tetlak, E. Heller, A. Crespo, R. Fitch, J. P. McCandless, K. Leedy, M. Baldini, G. Wagner, Z. Galazka, X. Li, and G. Jessen, Appl. Phys. Lett. **109**, 213501 (2016).

[30] Z. Hu, K. Nomoto, W. Li, Z. Zhang, N. Tanen, Q. T. Thieu, K. Sasaki, A. Kuramata, T. Nakamura, D. Jena, and H. G. Xing, Appl. Phys. Lett. **113**, 122103 (2018).

[31] W. Li, K. Nomoto, Z. Hu, D. Jena, and H. G. Xing, IEEE Trans. Electron Devices **68**, 2420–2426 (2021).

[32] Z. Jin, Y. Liu, N. Xia, X. Guo, Z. Hong, H. Zhang, and D. Yang, CrystEngComm **24**, 1127–1144 (2022).

[33] Z. Xi, Z. Liu, J. Fang, A. Bian, S. Zhang, J.-H. Zhang, L. Li, Y. Guo, and W. Tang, J. Phys. D: Appl. Phys. **57**, 493002 (2024).

[34] H.-K. Lee, H.-J. Yun, K.-H. Shim, H.-G. Park, T.-H. Jang, S.-N. Lee, and C.-J. Choi, Appl. Surf. Sci. **506**, 144673 (2020).

[35] X. Lu, T. Xu, Y. Deng, C. Liao, H. Luo, Y. Pei, Z. Chen, Y. Lv, and G. Wang, Appl. Surf. Sci. **597**, 153587 (2022).

[36] F. Zhang, X. Feng Zheng, Y. Hong Li, Z. Jian Yuan, S. Zhong Yue, X. Chen Wang, Y. Long He, X. Li Lu, X. Hua Ma, and Y. Hao, Appl. Surf. Sci. **684**, 161569 (2025).

[37] A. R. Gutierrez, J. A. Spencer, A. G. Jacobs, Y. Qin, J. R. Hajzus, H. N. Masten, E. Rocco, K. D. Hobart, T. J. Anderson, Y. Zhang, A. Kuramata, and M. J. Tadjer, J. Vac. Sci. Technol., A **43**, 033210 (2025).

[38] Y. Wang, G. Han, W. Xu, T. You, H. Hu, Y. Liu, X. Zhang, H. Huang, X. Ou, X. Ma, and Y. Hao, IEEE Trans. Electron Devices **69**, 1945–1949 (2022).

[39] H. Liu, J. Li, Y. Lv, Y. Wang, X. Lu, S. Dun, T. Han, H. Guo, A. Bu, X. Ma, Z. Feng, and Y. Hao, Appl. Phys. Lett. **121**, 202101 (2022).

[40] T. Oshima, Jpn. J. Appl. Phys. **64**, 088001 (2025).

[41] T. Oshima, Appl. Phys. Express **18**, 116501 (2025).

[42] Y. Zhang, A. Mauze, and J. S. Speck, Appl. Phys. Lett. **115**, 013501 (2019).

[43] C. Huang, W. Mu, H. Zhou, Y. Zhu, X. Xu, Z. Jia, L. Zheng, and X. Tao, RSC Adv. **8**, 6544–6550 (2018).

[44] S. Ohira and N. Arai, Phys. Status Solidi C **5**, 3116–3118 (2008).

[45] T. Oshima and Y. Oshima, Appl. Phys. Lett. **122**, 162102 (2023).

[46] R. J. Hoekstra, M. J. Kushner, V. Sukharev, and P. Schoenborn, J. Vac. Sci. Technol., B: Microelectron. Nanometer Struct.–Process., Meas., Phenom. **16**, 2102–2104 (1998).

[47] S. Rebollo, T. Itoh, S. Krishnamoorthy, and J. S. Speck, Appl. Phys. Lett. **125**, 012102 (2024).

[48] O. Ueda, N. Ikenaga, K. Koshi, K. Iizuka, A. Kuramata, K. Hanada, T. Moribayashi, S. Yamakoshi, and M. Kasu, Jpn. J. Appl. Phys. **55**, 1202BD (2016).

[49] Y. H. Choi, K. H. Baik, S. Kim, and J. Kim, Appl. Surf. Sci. **539**, 148130 (2021).